



Impact of hole transport material on perovskite solar cells with different metal electrode: A SCAPS-1D simulation insight

Eli Danladi^{a,*}, Philibus M. Gyuk^b, Nicholas N. Tasié^c, Anselem C. Egbugha^d, Debidatta Behera^e, Ismail Hossain^f, Ibrahim M. Bagudo^g, Mohammad L. Madugu^h, Jonathan T. Ikyumburⁱ

^a Department of Physics, Federal University of Health Sciences, Otuipo, Benue State, Nigeria

^b Department of Physics, Kaduna State University, Kaduna, Nigeria

^c Department of Physics, Rivers State University, Port Harcourt, Rivers State, Nigeria

^d Operations Unit, Starsight Energy, Nigeria

^e Department of Physics, Birla Institute of Technology, Mesra, Ranchi, 835215, India

^f School of Natural Sciences and Mathematics, Ural Federal University, Yekaterinburg, 620000, Russia

^g Department of Physics, Umaru Musa Yar'adua University, Katsina, Nigeria

^h Department of Physics, Gombe State University, Gombe, Nigeria

ⁱ Department of Physics, Benue State University, Makurdi, Nigeria

ARTICLE INFO

Keywords:

Perovskite solar cells
Defect density
HTM
Metal contact
SCAPS-1D

ABSTRACT

The high efficiency and low cost of production of perovskite solar cells (PSCs) based on organic-inorganic halides have attracted the attention of researchers. However, due to the intricacy in the synthesis of Spiro-OMeTAD and the high cost of gold (Au) utilized as the back contact (BC), have affected its viability for commercialization. In this present study, a simulation was performed with and without HTM utilizing different metal contacts (Ag, Cr, Cu, Au, Ni and Pt). SCAPS-1D, a software program in one dimension, was used to conduct the simulation. A systematic analysis was done to determine how the metal back contact's work functions affected the PSC both with and without HTM. The outcomes demonstrate that the PSCs' photovoltaic performance is significantly influenced by the metal contact's work function (W_F). The best metal contact for HTM and HTM-free devices was Pt, with a metal work function of 5.65 eV. The initial power conversion efficiencies (PCEs) for the two configurations were 26.229% for HTM-free and 25.608% for HTM-based device. A number of parameters, including absorber thickness, interface defect density, and electron transport material (ETM) thickness, were varied to obtain optimal values of 0.8 μm for both HTM and HTM-free PSCs, 10^{05} cm^{-2} for both HTM and HTM-free PSCs, and 0.01 μm for both HTM and HTM-free PSCs. These values were then used to simulate the final HTM and HTM-free devices with a PCE of 27.423%, current density (J_{sc}) of 27.546 mA/cm^2 , open circuit voltage (V_{oc}) of 1.239 V, and fill factor (FF) of 80.347% for HTM-free whereas PCE of 26.767% with J_{sc} of 27.545 mA/cm^2 , V_{oc} of 1.250 V, and FF of 77.733% for HTM based. These outcomes reflect outstanding enhancement of ~ 1.05 and ~ 1.07 times in PCE and J_{sc} over unoptimized cells with and without HTM.

* Corresponding author.

E-mail address: danladielibako@gmail.com (E. Danladi).

<https://doi.org/10.1016/j.heliyon.2023.e16838>

Received 24 March 2023; Received in revised form 28 May 2023; Accepted 30 May 2023

Available online 1 June 2023

2405-8440/© 2023 The Authors. Published by Elsevier Ltd. This is an open access article under the CC BY-NC-ND license (<http://creativecommons.org/licenses/by-nc-nd/4.0/>).

1. Introduction

At present, the demand of energy is satisfied by 80% of fossil fuel. However, it causes a serious depletion in crude reserves along with undesirable environmental effects as such prompted significant interest for alternative energy sources [1–4].

Perovskite Solar Cells as an alternative energy source can mitigate the problem connected to the energy crisis and global environment due to their unique properties that have attracted attention of researchers, among which include; high coefficient of absorption, outstanding carrier mobility, high diffusion length of electrons and holes, good carrier lifetime, low excitation binding energy, and large value of dielectric constant [5–7]. Since after its invention by Kojima et al. [8], a lot of investments in research have been done leading to a present certified record PCE exceeding 25% [5,9]. Despite all the achievements attained, there are still some factors that have rendered it incapacitated for commercial viability.

Studying the impact of the operating mechanism of a perovskite solar cell is essential to achieving the best performance possible. But there is still a lot of information about the interface band offset and the metal's W_F in perovskite solar cells that needs to be re-examined. In typical PSCs, a metal electrode is anticipated to have three main characteristics: (i) it shouldn't create a Schottky junction; (ii) it should have good conductivity; and (iii) it shouldn't react with the contact materials. Although Au (5.10 eV) is typically used as the back contact in PSC devices, other metals such as Ag (4.26 eV), C (5.00 eV), Cu (4.53 eV), W (4.32 eV), Al (4.28 eV), Ni (5.04 eV), Mo (4.36 eV), Ni (5.04 eV), and Pt (5.65 eV) have also been used and produced varied performance results [7,10–17]. The standard Au metal contact requires a high-technology manufacture and development procedure (like a high-vacuum evaporation technique), and Au reacts with iodine-containing perovskite compounds to generate $(AuI_2)^-$ and AuI_3 , which cause the gold electrode to degrade more quickly. Additionally, when perovskites, such as $MAPbI_3$, are decomposed by UV radiation, a quick reaction occurs with gold to form $MA_2Au_2I_6$, a phase with tetragonal symmetry that can infiltrate through HTM and contribute to the deterioration of the devices [18,19]. Most experimental researches done in PSCs are carried out without proper simulation to ascertain the optimized layers' properties before lab-scale development which can result to inferior device performance. Simulation and optimization are required to create a PSCs that is both highly efficient and ecologically friendly. Simulation is an essential tool for gaining a thorough understanding of the physical workings of solar cell devices, assessing the validity of given physical explanations, and determining the impact of physical modifications on performance. It can minimize not only the risk, time and money but also analyzes the attribute and role of layers to optimize the solar cell to best performance. Under optimized conditions, better metric parameters (J_{sc} , V_{oc} , FF and PCE) can be realized.

In this present paper, the effect of different metal contact with different work function was examined systematically through device simulation with Ni, Cu, Cr, Ag and Pt as metal electrodes. The PSCs under study were simulated with and without the HTM layer to see how metal's W_F affects recombination at the interfaces of perovskite and BC or at the interface of the HTM layer with BC. We studied how these interfacial events affect the cells' J_{sc} , V_{oc} , FF, and PCE.

Specifically, the experimental work demonstrated by Behrouznejad et al. [7] was considered for calibration in this work, where we used TiO_2 nanoparticles to aid the electron extraction, the perovskite nanocrystals ($CH_3NH_3PbI_3$) to produce e-h pairs when energetic photons are absorbed, and spiro-OMeTAD to extract holes. The device structure used in the simulation is as shown in Fig. 1. The W_F of the back contact is studied to determine their influence on the device performance. After assessing the most efficient device with its work function, the influence of absorber thickness, interface defect density and ETM thickness is explored in order to get an optimized value for the PCE. Based on the results presented we provided some useful guidance and recommendations in the design of lead-based PSCs, either with or without hole transport material.

2. Device simulation

In this article, solar cell capacitance simulator (SCAPS-1D) software was deployed as the tool to simulate the proposed device. Some simulation softwares for computational study apart from SCAPS-1D include; SILVACO ATLAS, COMSOL, AMPS-1D, SETFOS [13,

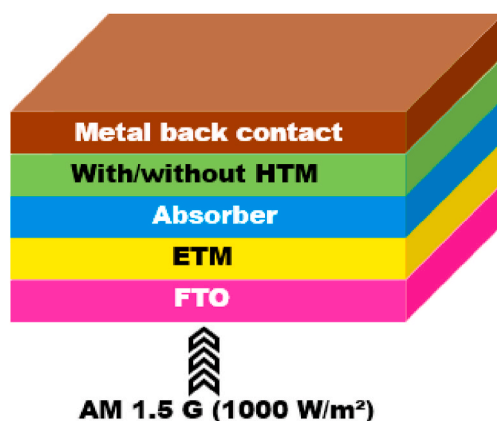


Fig. 1. The simulated device structure of the perovskite solar cell.

20–22]. Amongst the listed, SCAPS-1D has some advantages that made it subject of choice over others which include; user friendliness, simulation under the dark and under illumination conditions, and the fact that up to seven layer's heterojunction can be designed and simulated without routine measurements (C–V, C-f) [5]. The performance metrics of a solar cell such as PCE, FF, J_{sc} , and V_{oc} as well as the incident to photon conversion efficiency (IPCE), energy band gap can be predicted simply by solving the three basic equations of semiconductor (equations (1)–(3)) [5,23];

$$\frac{dp_n}{dt} = G_p - \frac{p_n - p_{n0}}{\tau_p} - p_n \mu_p \frac{dE}{dx} - \mu_p E \frac{dp_n}{dx} + D_p \frac{d^2 p_n}{dx^2} \quad (1)$$

$$\frac{dn_p}{dt} = G_n - \frac{n_p - n_{p0}}{\tau_n} - n_p \mu_n \frac{dE}{dx} - \mu_n E \frac{dn_p}{dx} + D_n \frac{d^2 n_n}{dx^2} \quad (2)$$

$$\frac{d}{dx} \left(-\varepsilon(x) \frac{d\psi}{dx} \right) = q [p(x) - n(x) + N_d^+(x) - N_a^-(x) + p_t(x) - n_t(x)] \quad (3)$$

where $N_d^-(x)$ and $N_d^+(x)$ denote the ionized donor doping concentration and the ionized acceptor doping concentration, respectively. Trapped holes are $p_t(x)$, while the free electrons are $n(x)$, and finally the free holes are $p(x)$. The electron charge is q , permittivity is ε , the electron diffusion coefficient is D , the rate of generation is G , the electric force field is E , the electron charge is q , and the electrostatic potential is ψ . Fig. 1 depicts the structure of the device, which consists of Ag, Cr, Cu, Au, Ni, and Pt as back contacts; spiro-OMeTAD as HTL; FTO as left contact; TiO_2 as ETL; and $CH_3NH_3PbI_3$ as a light-absorbing material.

This structure of PSC was used to study the effect of metal back contact in HTM based PSC with the purpose of obtaining the optimum metal contact for further optimization of layer's parameters. Same was done in the device without HTM. Ag = 4.47, Cr = 4.50, Cu = 4.65, Au = 5.10, Ni = 5.15, and Pt = 5.65 eV are the values of the work function for the various metal contacts. The basic structures' input parameters are listed in Tables 1 and 2.

3. Results and discussion

3.1. Metal back contact optimization in HTM and HTM-free devices

In perovskite solar cells, the metal work function of right contact is a crucial and fundamental factor for built-in voltage (V_{bi}). Different work functions of metal electrode are expected to give different performances. As such, it must be carefully chosen for device's optimum performance. In this sub-section, the simulation of HTM and HTM-free PSC was done with different metals (Ag, Cr, Cu, Au, Ni and Pt) and their performances were recorded. Fig. 2a & b shows the current-voltage (J - V) behavior of the devices without HTM and with HTM. For both devices, the performance was greatly affected by the type of metal contact used. The metal contact W_F ranged between 4.47 and 5.65 eV. Generally, Pt with metal W_F of 5.65 eV gave the best performance for both HTM free and HTM-based devices. In terms of the J_{sc} for HTM-based devices, the impact of BC is negligible for Au, Ni and Pt resulting to constant J_{sc} values. Fig. 2c & d shows the IPCE against wavelength for the HTM and HTM-free PSCs with different metal contact. The absorption extends throughout the entire visible spectrum and reaches a broad absorption maximum in the 350–820 nm range. The strong absorption at the visible region shows a satisfactory condition of our simulated device under 1sun light and agrees with similar studies with $MAPbI_3$ [24,25]. Tables 3 and 4 show the summary of the obtained results after the simulation. To ascertain the validity of our simulation, the results obtained were compared with experimental works depicted in Table 5 [7]. Since the simulation doesn't account for additional series resistances from BC, FTO, or the reflection of each layer and interface, FF and PCE for the simulated results were higher than experimental values [7]. Additionally, reasonable J_{sc} and V_{oc} that were in line with experimental findings were obtained, proving the viability of this simulation and illustrating how well the parameter corresponds to that of real devices. Another possible reason for the slight disparity in results is the method of preparation and deposition of the films [7,28,29]. According to some studies, $CH_3NH_3PbI_3$ is being investigated as an n-type semiconductor [30], while others reported $CH_3NH_3PbI_3$ as a p-type semiconductor [31–35]. By Yin et al. [36], It was shown that $CH_3NH_3PbI_3$ had shallow levels that determined the semiconductor type (p or n), as well as p-type

Table 1
PSC device simulation data [10,20–27].

Parameters	FTO	ETM (TiO_2)	Absorber	HTM
Thickness (μm)	0.4	0.05	0.45	0.35
E_g (eV)	3.5	3.20	1.50	3.0
E_g (eV)	4.0	4.2	3.9	2.45
χ	9	10	6.5	3.0
N_C (cm^{-3})	2.2×10^{18}	2.2×10^{18}	2.2×10^{18}	2.5×10^{18}
N_V (cm^{-3})	2.2×10^{18}	2.2×10^{18}	2.2×10^{18}	1.8×10^{19}
μ_n ($cm^2 V^{-1} s^{-1}$)	20	20	2	2×10^{-4}
μ_p ($cm^2 V^{-1} s^{-1}$)	10	10	2	2×10^{-4}
N_D (cm^{-3})	1×10^{19}	1×10^{17}	0	0
N_A (cm^{-3})	0	0	1×10^{13}	1×10^{18}
N_t (cm^{-3})	1×10^{15}	1×10^{15}	2.5×10^{13}	1×10^{15}

Table 2
Absorber and interface defect parameters [25,27].

Parameters	TiO ₂ /MAPbI ₃ interface	MAPbI ₃ /Spiro-OMeTAD interface
Defect type	Neutral	Neutral
Capture cross section for electrons (cm ²)	1×10^{-19}	1×10^{-19}
Capture cross section for holes (cm ²)	1×10^{-19}	1×10^{-19}
Energetic distribution	Single	Single
Energy level with respect to Ev (eV)	0.650	0.650
Characteristic energy (eV)	0.1	0.1
Total density (cm ⁻³)	1×10^{10}	1×10^{10}

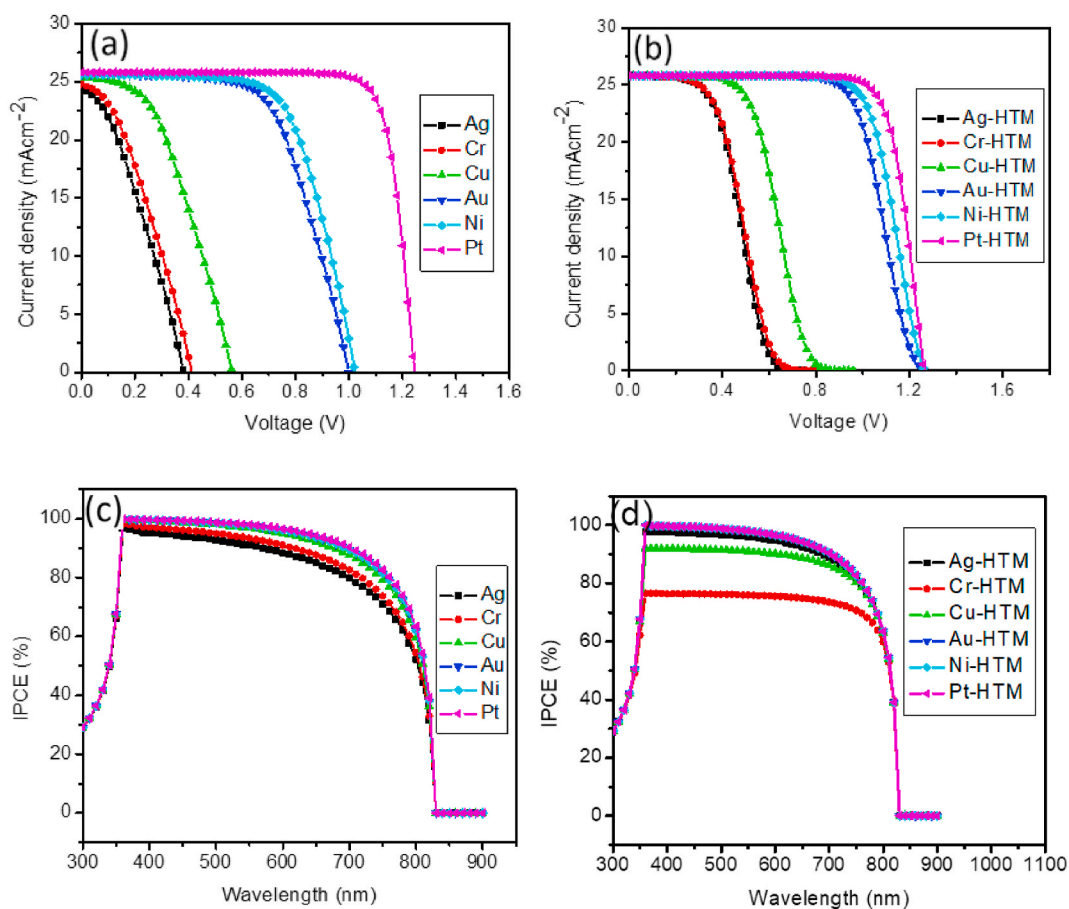


Fig. 2. (a) *J-V* curve with different metal contact under illumination without HTM, (b) *J-V* curve with different metal contact under illumination with HTM, (c) QE with respect to wavelength for HTM-free PSC and (d) QE with respect to wavelength for HTM-based PSC.

Table 3
J-V characteristic parameters with different metal contact for HTM-free PSC.

Metal	PCE (%)	FF (%)	J_{sc} (mA/cm ²)	V_{oc} (V)
Ag	3.108	33.201	24.513	0.382
Cr	3.586	35.098	24.799	0.412
Cu	6.338	44.501	25.347	0.562
Au	16.166	63.152	25.618	0.999
Ni	17.311	65.984	25.629	1.024
Pt	26.229	81.596	25.781	1.247

Table 4
J-V characteristic parameters with different metal contact for HTM-based PSC.

Metal	PCE (%)	FF (%)	J_{sc} (mA/cm ²)	V_{oc} (V)
Ag-HTM	8.527	42.694	25.774	0.775
Cr-HTM	8.630	42.193	25.774	0.794
Cu-HTM	12.054	49.626	25.781	0.942
Au-HTM	22.768	69.908	25.782	1.263
Ni-HTM	23.941	73.491	25.782	1.264
Pt-HTM	25.608	78.601	25.782	1.264

Table 5
J-V characteristic parameters of HTM-free and HTM-based PSC [7].

Sample	J_{sc} (mA/cm ²)	V_{oc} (V)	FF (%)	PCE (%)
Au	4.85	0.809	65.38	2.46
Ag	4.93	0.087	39.34	0.17
Pt	7.17	0.686	62.60	3.08
Ni	8.52	0.411	49.92	1.75
Cu	10.42	0.301	33.69	1.06
Cr	0.89	0.753	21.83	0.14
Au-HTM	20.99	1.0091	77.60	16.44
Ag-HTM	20.60	1.023	78.32	16.51
Pt-HTM	20.58	1.006	71.07	14.72
Ni-HTM	18.21	0.834	51.61	7.83
Cu-HTM	20.32	0.942	47.89	9.17
Cr-HTM	0.47	0.04	18.41	0.04

vacancies connected to Pb and n-type vacancies connected to CH_3NH_3^+ . We can hypothesize that high energy loss occurs during hole transfer to various metal back contacts after metal deposition on $\text{CH}_3\text{NH}_3\text{PbI}_3$ film or spiro-OMeTAD film as a result of the energy offset between $\text{CH}_3\text{NH}_3\text{PbI}_3$'s valence band edge and the system's Fermi level, which is thought to be one of the main causes of the significant discrepancy between the experimental and simulated results. Miller et al. [37] have demonstrated that the preparation technique affects the work function of the perovskite layer. Surface contamination and the method of measurement are additional factors [7]. This leads to the conclusion that the $\text{CH}_3\text{NH}_3\text{PbI}_3$ layer's charge carrier density is low in their experimental work and that under the impact of that underlayer's carrier density, the work function changes depending on the preparation and deposition processes. This by implication means that $\text{CH}_3\text{NH}_3\text{PbI}_3$ practically behaves like an intrinsic semiconductor.

The recombination rate at the interface of metal (Ag, Cr, Cu, Au, and Ni) and spiro-OMeTAD was higher than the recombination rate at the interface of metal (Ag, Cr, Cu, Au, and Ni) and $\text{CH}_3\text{NH}_3\text{PbI}_3$ which can be depicted in Fig. 3a and b. For Pt, the internal resistance is substantially larger when HTM is inserted than when it is not. This has proven that the spiro-OMeTAD and Pt metal electrodes have significant interfacial resistances, which leads to formation of non-ohmic contact. Using Mo metal contact on spiro-OMeTAD with a work function of 4.6 eV has been demonstrated to cause the contact metal atoms to penetrate the spiro-OMeTAD layer and produce non-ohmic contact with $\text{CH}_3\text{NH}_3\text{PbI}_3$, which increases series resistance and results in an S-shaped *J-V* curve [38]. We can clearly detect the S-shape *J-V* curve in our data in Fig. 2b for Cu since it has the same work function of 4.6 eV and close values of work function for Cr and Ag in the current study. This behavior can be attributed to the penetration of Cu, Cr and Ag atoms through the HTM. It can now be concluded that the spiro-OMeTAD used in our simulation is not a good hole transport material when

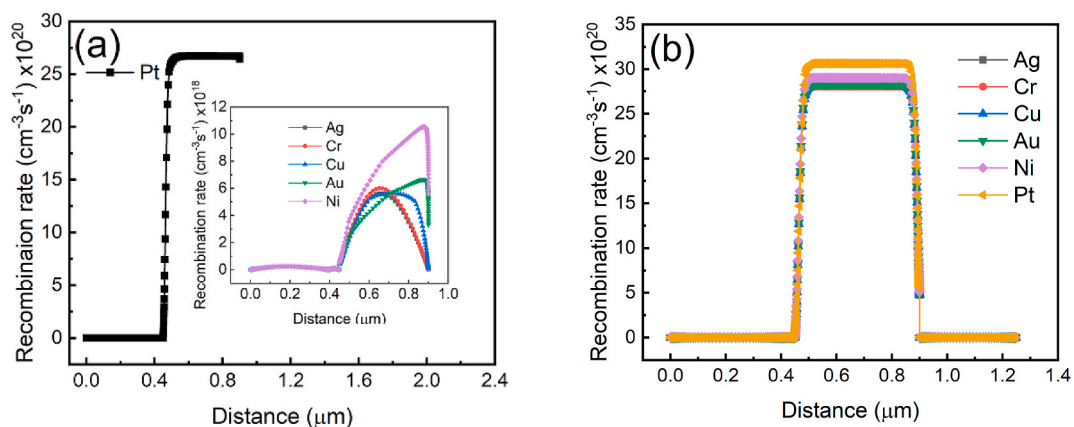


Fig. 3. The recombination rate of PSC with different metal back contact based on (a) HTM-free and (b) HTM-based device.

Cu, Cr and Ag are used as metal contact.

It can further be confirmed from the IPCE against wavelength plot for the HTM based devices with Cu, Cr and Ag as metal contact that their quantum efficiencies were below 100% with Cr having 76%, Cu having 92.04% and Ag having 98.07%. In the case of the HTM-free devices, the quantum efficiencies were enhanced with spiro-OMeTAD elimination resulting to IPCE value of 97.08, 98.01 and 99% for Ag, Cr and Cu.

Having obtained the optimal back contact to be Pt with W_F of 5.65 eV, we focus on optimizing the thickness of the absorber, ETM thickness, the interface defect between the absorber and the ETM for HTM-free and the interface defect between the absorber and ETM, and between the absorber and HTM for HTM-based.

Fig. 4a & b shows the best HTM-free device and its corresponding energy profile. The energy profile demonstrates the effective role of the W_F of the metal contact. The photogenerated electrons and holes that are generated in the conduction band with offset (0.26 eV) and the valence band with offset (1.90 eV) are highly beneficial and are expected to allow or/block the careers respectively. TiO_2 has a conduction band energy of ~ -4.0 eV and a deep valence band energy of about -7.3 eV which makes it an ideal material for electron selectivity in PSCs [7,32]. In this scenario, it is anticipated that the metal contact will capture photo-generated holes.

With the insertion of HTM (spiro-OMeTAD), the HOMO of the HTM collects the holes and a relatively high V_{oc} is maintained due to the increase in the built in voltage caused by the insertion. Hence, deeper HOMO results in larger V_{oc} [39]. Thus, the HTM is essential in maintaining a high V_{oc} ; consequently, the FF increases significantly to complement the high V_{oc} as shown in Table 3. In a practical term, the HTM is capable of preventing short circuiting in PSC by forming a shell layer between the absorber nanocrystals and the metal [40].

Fig. 4c shows the J - V curve for an HTM device with a different back contact while Fig. 4d shows the energy band gap profile of the HTM-based device. The MAPbI_3 /Spiro-OMeTAD has a valence band offset (VBO) of 0.05 eV. A barrier in the passage of photo-generated holes from MAPbI_3 to HTM results from a larger value of VBO. Because the VBO in this work was so low, spiro-OMeTAD was a good choice for the HTM with Pt metal contact. The VBO value needs to be low to allow holes from the MAPbI_3 to enter the HTM, and it shouldn't be high enough to generate an accumulation of holes at the absorber/HTM interface that may trigger recombination [41]. As a result, it's critical to take into account a material with a low negative or value VBO for improved band

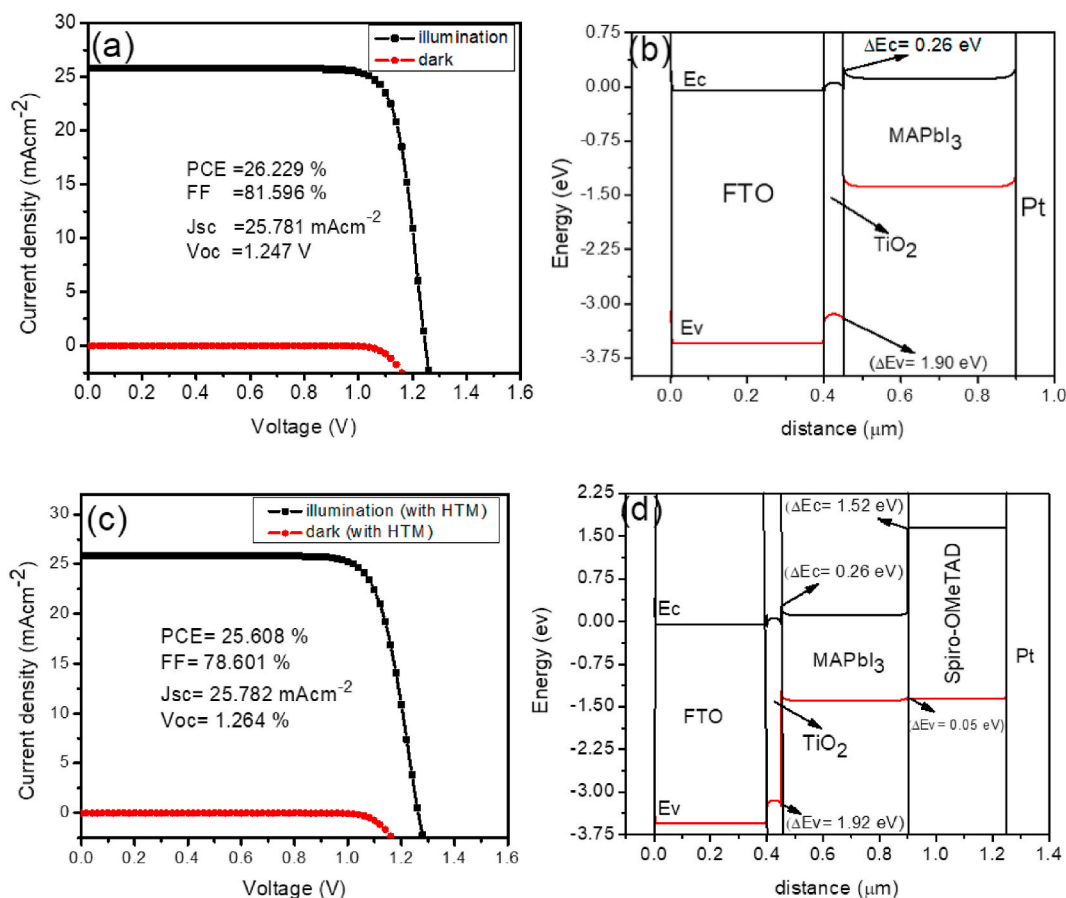


Fig. 4. (a) J - V curve for optimal metal contact without HTM in the light and the dark, (b) Energy profile diagram of the device with optimal metal contact without HTM, (c) J - V curve in the light and the dark for optimal metal contact with HTM and (d) Device energy profile diagram with optimal metal contact with HTM.

alignment, which will ultimately lead to improved device performance. The metric parameters for the Pt-metal device with HTM gave $V_{oc} = 1.264$ V, $J_{sc} = 25.782$ mA/cm², FF = 78.601%, and PCE = 25.608%.

3.2. Influence of absorber thickness in devices with and without HTM

The performance properties of PSCs are significantly influenced by the thickness of MAPbI₃. The thickness needs to be chosen in such a way that it will not be too thick no thin. The diffusion lengths and lifetime of photogenerated carriers are affected by absorber layer thickness [42]. A simulation was run with an absorber layer thickness range of 0.1–1.3 μm to better understand the impact of perovskite thickness on the metrics of perovskite solar cells. For both HTM-free and HTM-based devices, Fig. 5a–d and 6a–d display the *J*-*V* characteristic curve, IPCE vs. wavelength plots, and variation of the metric parameters with absorber layer thickness. The variation of metric parameters with different thickness values are shown in Fig. 5c and d and 6c & d. As shown in Figs. 5a & 6a, increase in the perovskite thickness from 0.1 to 0.8 μm results to rapid increase in PCE from 14.718 to 27.154% for HTM-free and from 14.630 to 26.436% for HTM-based. Beyond 0.8 μm, there was a decrease in PCE. The V_{oc} and J_{sc} increases rapidly with increase in absorber thickness for both configurations. FF drastically decreases at the same time to counterbalance the high V_{oc} and J_{sc} , bringing about slightly higher PCE. The enhanced increase in PCE up to 0.8 μm is attributed to a high absorption coefficient of the devices observed in this range of spectrum [25]. Therefore, the optimal thickness of the MAPbI₃ in our research work was 0.8 μm and as such considered for further simulation. The device performance for the HTM-free at that optimal value is as follows: PCE = 27.154%, FF = 79.910%, $J_{sc} = 27.546$ mA/cm², and $V_{oc} = 1.234$ V (Table 6) and for the device performance for the HTM-based is as follows: PCE = 26.436%, FF = 77.267%, $J_{sc} = 27.546$ mA/cm², and $V_{oc} = 1.242$ V (Table 7).

From the results, it shows that the elimination of the HTM was slightly beneficial to the efficiency enhancement. To support this statement, in practical terms, it was demonstrated that after depositing Au metal contact on MAPbI₃ film, the energy offset between valence band edge of MAPbI₃ and the Fermi level of the system was found to be 0.6 eV which leads to low energy loss during the process of transferring hole to the metal right contact (Au) [7]. Thus, irrespective of the existence of HTM or not, the choice of the absorber thickness is crucial in realizing high PCE.

The IPCE against wavelength curves for both devices with HTM and without HTM shows increase in quantum efficiencies with increase in the absorber thickness. The QE increases from 80% at (0.1 μm) to 100% at (1.3 μm). The strong QE is due to increase in

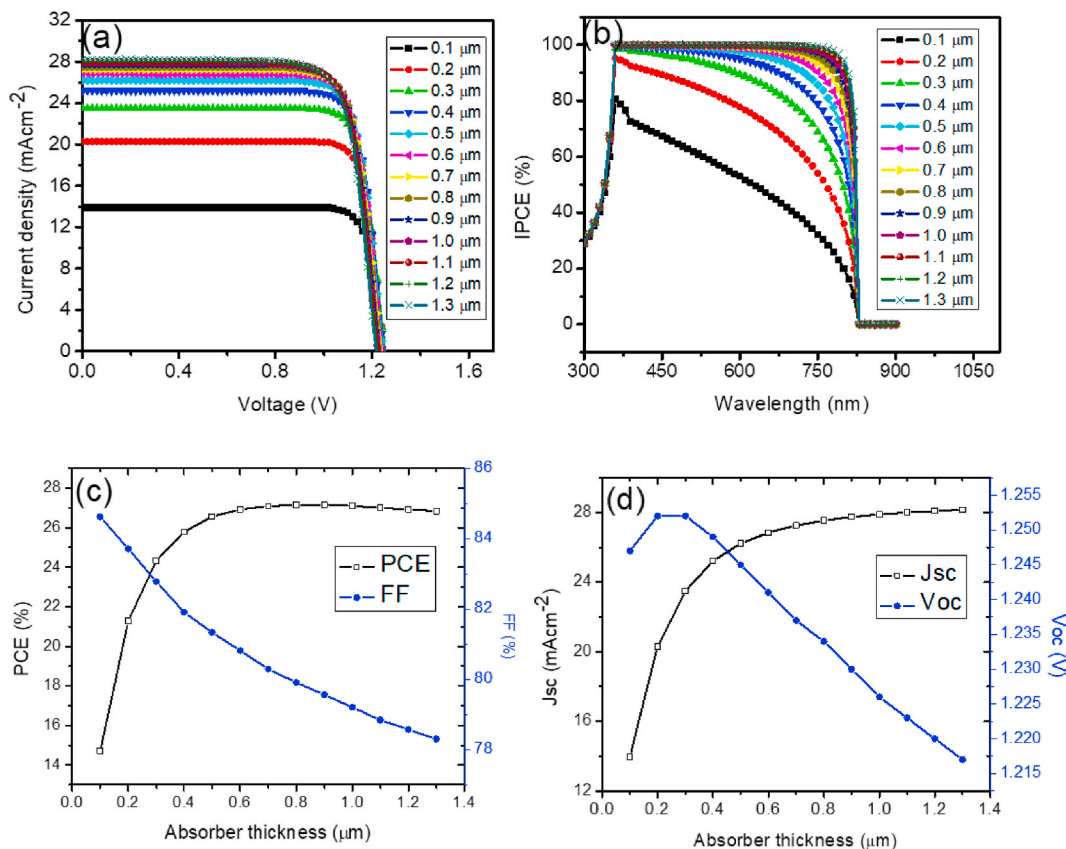


Fig. 5. (a) *J*-*V* curve with varying thickness of absorber in the light condition, (b) QE vs. wavelength, (c) PCE and FF vs. thickness of absorber and (d) J_{sc} and V_{oc} vs. absorber thickness for PSCs without HTM.

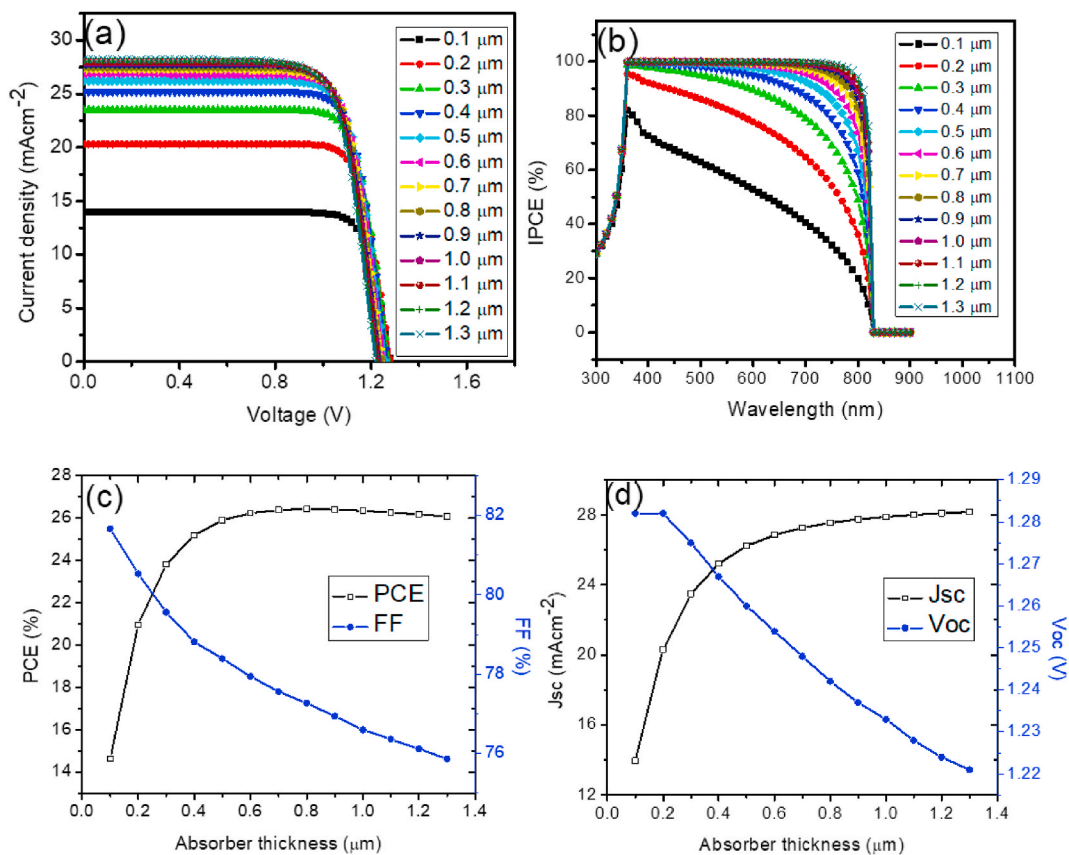


Fig. 6. (a) J - V curve with varying thickness of absorber in the light condition, (b) QE vs. wavelength, (c) PCE and FF vs. thickness of absorber and (d) J_{sc} and V_{oc} vs. absorber thickness for PSCs with HTM.

Table 6

J - V characteristic data without HTM with varying absorber thickness.

Thickness (μm)	PCE (%)	FF (%)	J_{sc} (mAcm ⁻²)	V_{oc} (V)
0.1	14.718	84.617	13.950	1.247
0.2	21.278	83.711	20.296	1.252
0.3	24.327	82.777	23.482	1.252
0.4	25.786	81.907	25.213	1.249
0.5	26.552	81.331	26.223	1.245
0.6	26.930	80.816	26.851	1.241
0.7	27.085	80.293	27.263	1.237
0.8	27.154	79.910	27.546	1.234
0.9	27.152	79.562	27.748	1.230
1.0	27.097	79.206	27.897	1.226
1.1	27.004	78.840	28.010	1.223
1.2	26.926	78.574	28.098	1.220
1.3	26.835	78.302	28.168	1.217

extinction coefficient as the thickness increases.

3.3. ETL/absorber interface defect for HTM-free

The ETL/absorber interface flaw adversely affects the PSC device's performance. To examine the performance of PSC in a more realistic way, ETL/absorber interface density (N_f) was introduced in our initial device ranging from 10^5 to 10^{12} cm⁻², attempt to exceed above 10^{12} cm⁻² leads to convergence failure. Though the values chosen are somewhat too low in practical terms but it's necessary to elucidate its significance in theoretical basis. At the ETL/absorber interface, the N_f affects the stability and performance properties of PSCs. Fig. 7a–d shows the J - V characteristics plot, IPCE-wavelength plot and variation in device parameters with diverse defect densities of ETL/absorber interface, PCE and FF maintains a constant value at 10^5 and 10^6 cm⁻² before they start decreasing.

Table 7
J-V characteristic data with HTM with varying absorber thickness.

Thickness (μm)	PCE (%)	FF (%)	J_{sc} (mA/cm^2)	V_{oc} (V)
0.1	14.630	81.670	13.968	13.968
0.2	20.952	80.530	20.302	20.302
0.3	23.821	79.563	23.485	23.485
0.4	25.185	78.815	25.214	25.214
0.5	25.903	78.389	26.224	26.224
0.6	26.236	77.940	26.851	26.851
0.7	26.381	77.559	27.263	27.263
0.8	26.436	77.267	27.546	27.546
0.9	26.412	76.942	27.748	27.748
1.0	26.338	76.595	27.897	27.897
1.1	26.271	76.358	28.010	28.010
1.2	26.185	76.116	28.098	28.098
1.3	26.082	75.858	28.168	28.168

The V_{oc} also maintains a linear variation up to 10^{08} cm^{-2} before it starts decreasing. The drop in device characteristics may be explained by the fact that electrons moving from the MAPbI₃ layer to TiO₂ are more likely to be trapped or quenched as a result of recombination as the N_t at the ETL/absorber interface increases. Though there are three defect density (10^{05} , 10^{06} , and 10^{07} cm^{-2}) with the same performance as shown in Table 8, so ETL/absorber defect density of a value equal to or less than 10^{07} cm^{-2} gives reasonable performance. But it is often impractical to realize a very low ETL/absorber defect, so we chose 10^{07} cm^{-2} as optimized value for further simulations. The performance of the device at 10^{07} cm^{-2} ETL/absorber defect density is as follows: $V_{oc} = 1.254 \text{ V}$, $J_{sc} = 25.781 \text{ mA}/\text{cm}^2$, $FF = 82.277\%$ and $PCE = 26.596\%$.

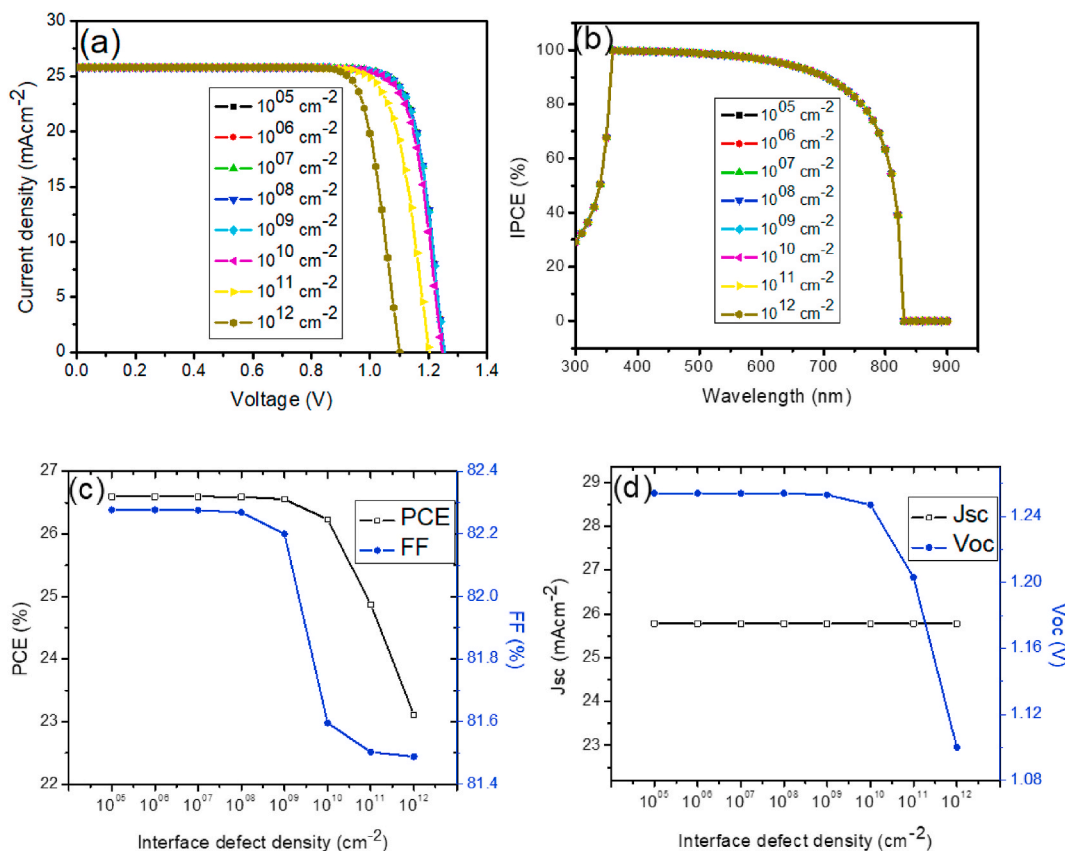


Fig. 7. (a) *J-V* curve with varying ETL/absorber interface defect density in the light condition, (b) QE vs. wavelength, (c) PCE and FF vs. ETL/absorber interface defect density and (d) J_{sc} and V_{oc} vs. ETL/absorber interface defect density for PSCs without HTM.

Table 8
J-V characteristic data without HTM with varying ETL/absorber interface defect density.

N_t (cm^{-2})	PCE (%)	FF (%)	J_{sc} (mAcm^{-2})	V_{oc} (V)
10^{05}	26.596	82.277	25.781	1.254
10^{06}	26.596	82.277	25.781	1.254
10^{07}	26.596	82.276	25.781	1.254
10^{08}	26.592	82.269	25.781	1.254
10^{09}	26.556	82.200	25.781	1.253
10^{10}	26.229	81.596	25.781	1.247
10^{11}	24.868	81.503	25.781	1.203
10^{12}	23.109	81.488	25.781	1.100

3.4. ETL/absorber interface defect and HTM/absorber interface defect for HTM-base

The ETL/absorber interface flaw significantly affects the PSC device performance. To examine the performance of PSC in a more realistic way, ETL/absorber interface density was introduced in our initial device with variation values from 10^{05} to 10^{12} cm^{-2} . At the ETL/absorber interface, the N_t affects the stability and performance properties of PSCs with HTM since the structures are also made up of discontinues materials. Fig. 8a–d shows the *J-V* characteristics plot, IPCE-wavelength plot with diverse ETL/absorber interface defect densities, *J-V* characteristics plot of absorber/HTM interface defect densities and IPCE-wavelength plot with absorber/HTM interface defect densities. PCE and FF maintains a constant value at 10^{05} and 10^{06} cm^{-2} before they start decreasing. The V_{oc} also maintains a linear variation up to 10^{08} cm^{-2} before it starts decreasing. The drop in device characteristics may be explained by the fact that electrons moving from the MAPbI₃ layer to the ETL are more likely to be caught or quenched as a result of recombination as the N_t at the ETL/absorber interface increases. Despite the fact that three ETL/absorbers have the same performance as shown in Table 9, therefore, a defect density for ETL/absorbers equal to or below 10^{07} cm^{-2} results in acceptable performance. However, it is frequently impracticable to achieve a very small ETL or absorber defect, so we chose 10^{07} cm^{-2} as optimized value for further simulations. The performance of the device at 10^{07} cm^{-2} ETL/absorbers defect density is as follows: $V_{oc} = 1.277$ V, $J_{sc} = 25.782$ mA/cm², FF = 78.943% and PCE = 25.991%.

Additionally, the PSC performance and stability are impacted by the N_t at the absorber/HTM contact. The device was simulated with by changing the absorber/HTM N_t from 10^{05} to 10^{12} cm^{-2} . As shown in Fig. 8c and d, varying the defect density at the absorber/HTL interface has no effect on the performance metrics of the device (see Table 10). The IPCE versus wavelength curve exhibits spectral overlap when the absorber/HTL N_t is chosen between 10^{05} to 10^{12} cm^{-2} , which is explained by unchanging optical absorption efficiency at the chosen values of the absorber/HTM defect density.

3.5. ETL thickness with and without HTM

In order to examine how performance is impacted by ETL thickness of PSCs with HTM and without HTM, the thickness of the ETL was varied from 0.01 to 0.10 μm . Fig. 9a–d and 10a–d show the *J-V* curves, IPCE-wavelength, and photovoltaic parameters with respect to the varied thickness on device without HTM and with HTM. With ETL thickness increased, the J_{sc} and V_{oc} were unaffected. The PCE and FF slightly decreases with increased thickness. The decrease in PCE and FF can be attributed to the series resistance offered by the layer thickness. The QE versus wavelength curve exhibits spectrum overlap when the thickness is chosen between 0.01 and 0.10 μm , which is explained by the unchanged optical absorption efficiency for the chosen thickness values. The optimal ETL thickness was 0.01 μm for both HTM-free and HTM-based devices. The parameters at the optimal values are as follows: (PCE = 26.396%, FF = 82.123%, $J_{sc} = 25.781$ mA/cm² and $V_{oc} = 1.247$ V) (Table 11) for device without HTM and (PCE = 25.764%, FF = 79.091%, $J_{sc} = 25.782$ mA/cm² and $V_{oc} = 1.263$ V) (Table 12) for device with HTM.

3.6. Optimized device

After careful variation of the selected ranged parameters, we obtained 0.8 μm for MAPbI₃ thickness for both devices without HTM and with HTM, 10^{07} cm^{-2} for TiO₂/MAPbI₃ interface defect density for both devices without HTM and with HTM, 10^{07} cm^{-2} MAPbI₃/HTM interface defect density for device with HTM, 0.01 μm for TiO₂ thickness for both devices without HTM and with HTM. The optimized parameters were used to simulate the final device with and without HTM.

Fig. 11 depicts the *J-V* characteristics and IPCE-wavelength curve for the optimized device with and without HTM. The performance of both devices gave optimal parameters as follows: $V_{oc} = 1.239$ V, $J_{sc} = 27.546$ mA/cm², FF = 80.347% and PCE = 27.423% for device without HTM and $V_{oc} = 1.250$ V, $J_{sc} = 27.545$ mA/cm², FF = 77.733% and PCE = 26.767% for device with HTM.

The outcomes suggest an outstanding improvement of ~ 1.05 and ~ 1.07 times in PCE and J_{sc} over the unoptimized cell without HTM, and ~ 1.05 and ~ 1.07 times in PCE and J_{sc} against the unoptimized cell with HTM. Both devices experienced the same enhancement strength. Thus, irrespective of whether there is HTM or not, the enhancement power remains same.

Table 13 shows the comparison of results obtained in this study via simulation with other previously published works to validate our findings and its applicability in research. The results obtained are encouraging and have highlighted the prospect of the proposed structure and emphasize the importance of using HTM-free solar cells without deteriorating the efficiency.

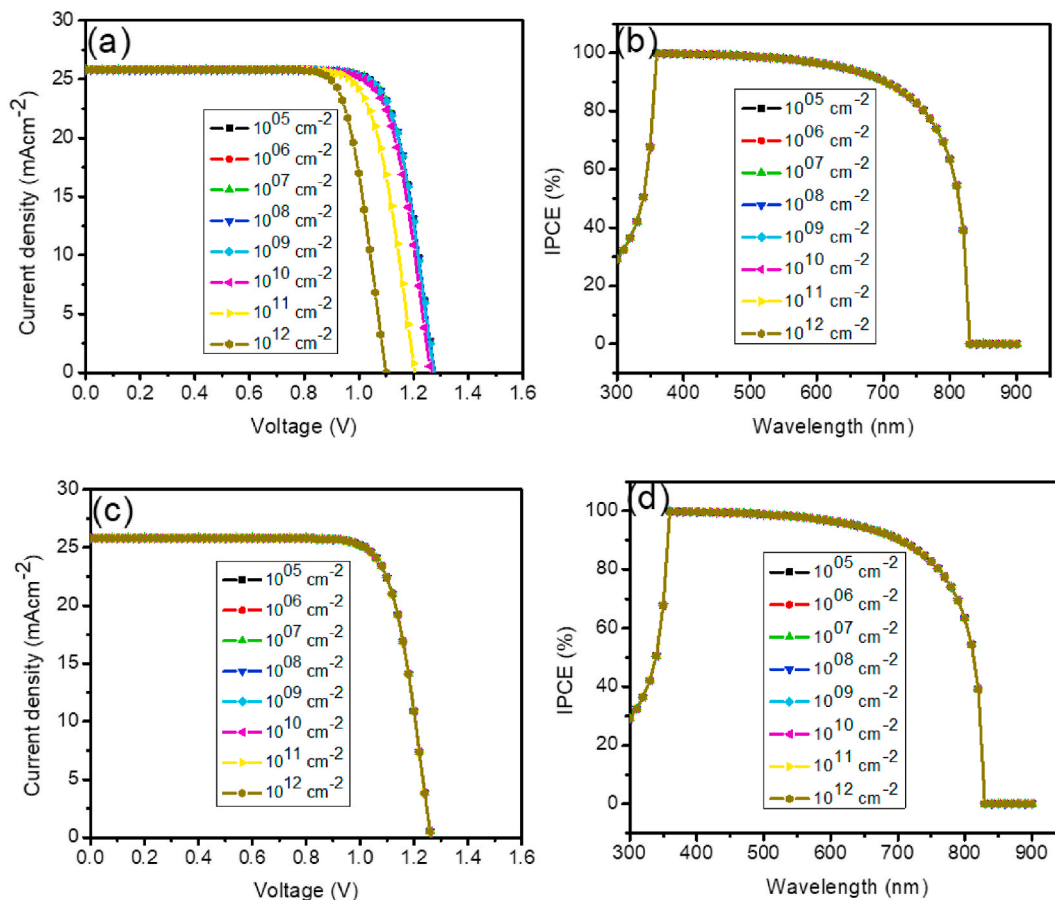


Fig. 8. (a) *J-V* curve with varying ETL/absorber interface defect density in the light condition, (b) QE vs. wavelength of ETL/absorber interface defect density (c) *J-V* curve with varying absorber/HTM interface defect density in the light condition and (d) QE vs. wavelength of absorber/HTM interface defect density for PSCs with HTM.

Table 9

J-V characteristic data with HTM with varying ETL/absorber interface defect density.

N_t (cm ⁻²) (ETM-Abs)	PCE (%)	FF (%)	J_{sc} (mA/cm ²)	V_{oc} (V)
10 ⁰⁵	25.991	78.943	25.782	1.277
10 ⁰⁶	25.991	78.943	25.782	1.277
10 ⁰⁷	25.991	78.943	25.782	1.277
10 ⁰⁸	25.986	78.939	25.782	1.277
10 ⁰⁹	25.947	78.902	25.782	1.276
10 ¹⁰	25.608	78.601	25.782	1.264
10 ¹¹	24.216	77.922	25.782	1.205
10 ¹²	22.451	79.166	25.782	1.100

Table 10

J-V characteristic data with HTM with varying absorber/HTM interface defect density.

N_t (cm ⁻²) (Abs-HTM)	PCE (%)	FF (%)	J_{sc} (mA/cm ²)	V_{oc} (V)
10 ⁰⁵	25.608	78.601	25.782	1.264
10 ⁰⁶	25.608	78.601	25.782	1.264
10 ⁰⁷	25.608	78.601	25.782	1.264
10 ⁰⁸	25.608	78.601	25.782	1.264
10 ⁰⁹	25.608	78.601	25.782	1.264
10 ¹⁰	25.608	78.601	25.782	1.264
10 ¹¹	25.608	78.601	25.782	1.264
10 ¹²	25.608	78.601	25.782	1.264

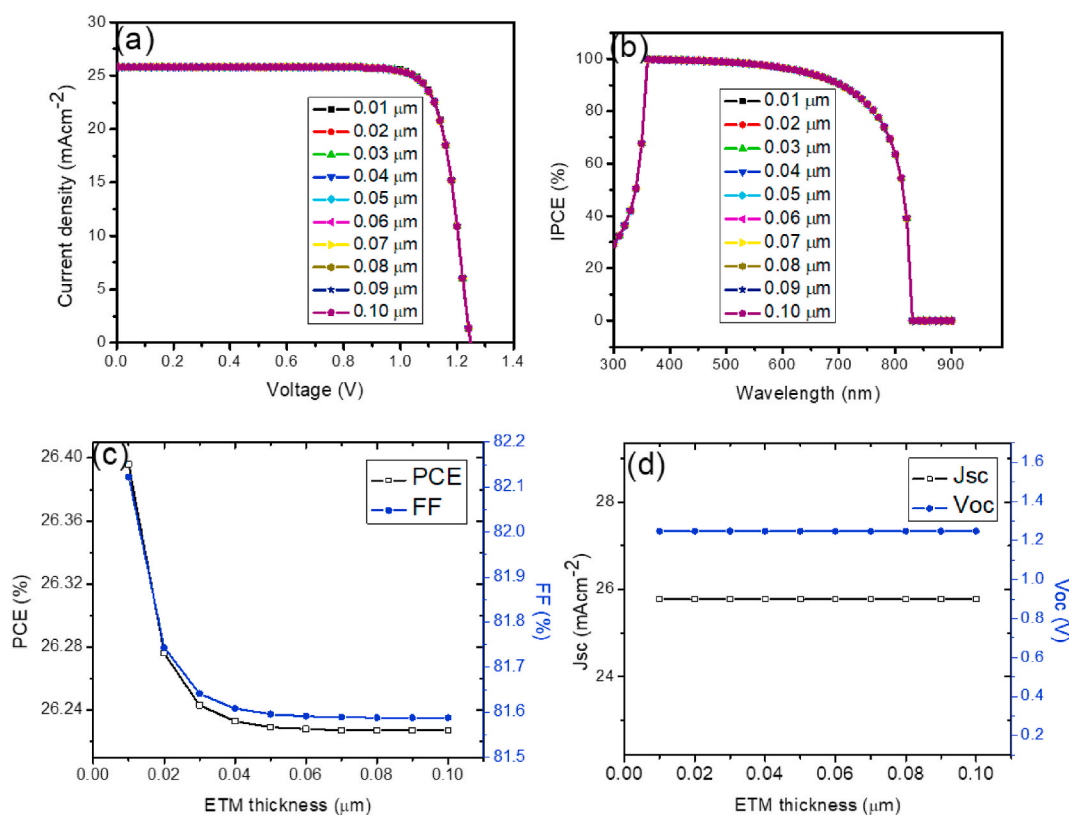


Fig. 9. (a) J - V curve with varying ETL thickness in the light condition, (b) QE vs. wavelength, (c) PCE and FF vs. ETL thickness and (d) J_{sc} and V_{oc} vs. ETL thickness for PSCs without HTM.

4. Conclusion

In this present work, the impact of metal contact on HTM and HTM-free PSC was first studied to obtain the optimal work function. With the control of thickness of absorber layer (0.1–1.3 μm), interface defect density from 10^{05} - 10^{12} cm⁻², and ETM thickness from 0.01 to 0.10 μm for both HTM and HTM-free perovskite solar cells, their effects were investigated through optimization to obtain the final optimized devices using SCAPS-1D simulation tool. The optimized device without HTM revealed the efficiency of power conversion of 27.423%, with 80.347% of fill factor, current density of 27.546 mA/cm², voltage of 1.239 V and maximum quantum efficiency of 100% in the visible range whereas the device with HTM demonstrated a power conversion efficiency of 26.767%, fill factor of 77.733%, current density of 27.545 mA/cm², voltage of 1.250 V and also a maximum incident to photon conversion efficiency of 100% in the visible region. These results show an improvement of ~ 1.05 and ~ 1.07 times in PCE and J_{sc} over the unoptimized cells with and without HTM. The results obtained are impressive and have demonstrated the prospect of alternative metal back contact other than Au and have indicated the possibility of efficiency enhancement on simplified structures.

Funding

This article did not receive any funding support.

Author contribution statement

Eli Danladi: conceived and designed the experiments; performed the experiments; analyzed and interpreted the data; contributed reagents, materials, analysis tools or data; wrote the paper.

Philibus M. Gyuk: performed the experiments; analyzed and interpreted the data; contributed reagents, materials, analysis tools or data.

Nicholas N. Tasie: conceived and designed the experiments; analyzed and interpreted the data; contributed reagents, materials, analysis tools or data.

Anselem C. Egbugha; Debidatta Behera; Ismail Hossain; Ibrahim M. Bagudo; Mohammad L. Madugu; Jonathan T. Ikyumbur: analyzed and interpreted the data; contributed reagents, materials, analysis tools or data.

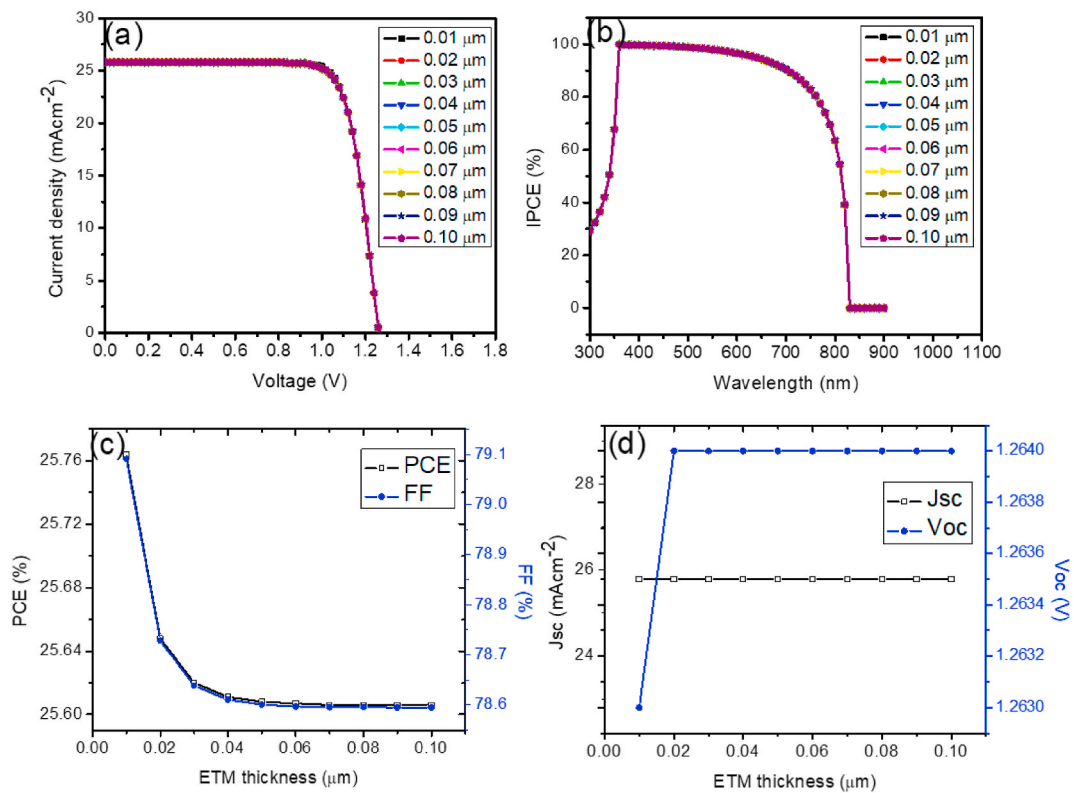


Fig. 10. (a) *J*-*V* curve with varying ETL thickness in the light condition, (b) QE vs. wavelength, (c) PCE and FF vs. ETL thickness and (d) *J*_{sc} and *V*_{oc} vs. ETL thickness for PSCs with HTM.

Table 11

J-*V* characteristic data without HTM with varying ETL thickness.

Thickness (μm)	PCE (%)	FF (%)	<i>J</i> _{sc} (mA/cm ²)	<i>V</i> _{oc} (V)
0.01	26.396	82.123	25.781	1.247
0.02	26.276	81.744	25.781	1.247
0.03	26.243	81.641	25.781	1.247
0.04	26.233	81.608	25.781	1.247
0.05	26.229	81.596	25.781	1.247
0.06	26.228	81.591	25.781	1.247
0.07	26.227	81.589	25.781	1.247
0.08	26.227	81.588	25.781	1.247
0.09	26.227	81.588	25.781	1.247
0.10	26.227	81.588	25.781	1.247

Table 12

J-*V* characteristic data with HTM with varying ETL thickness.

Thickness (μm)	PCE (%)	FF (%)	<i>J</i> _{sc} (mA/cm ²)	<i>V</i> _{oc} (V)
0.01	25.764	79.091	25.782	1.263
0.02	25.648	78.729	25.782	1.264
0.03	25.62	78.639	25.782	1.264
0.04	25.611	78.611	25.782	1.264
0.05	25.608	78.601	25.782	1.264
0.06	25.607	78.597	25.782	1.264
0.07	25.606	78.596	25.782	1.264
0.08	25.606	78.596	25.782	1.264
0.09	25.606	78.595	25.782	1.264
0.10	25.606	78.595	25.782	1.264

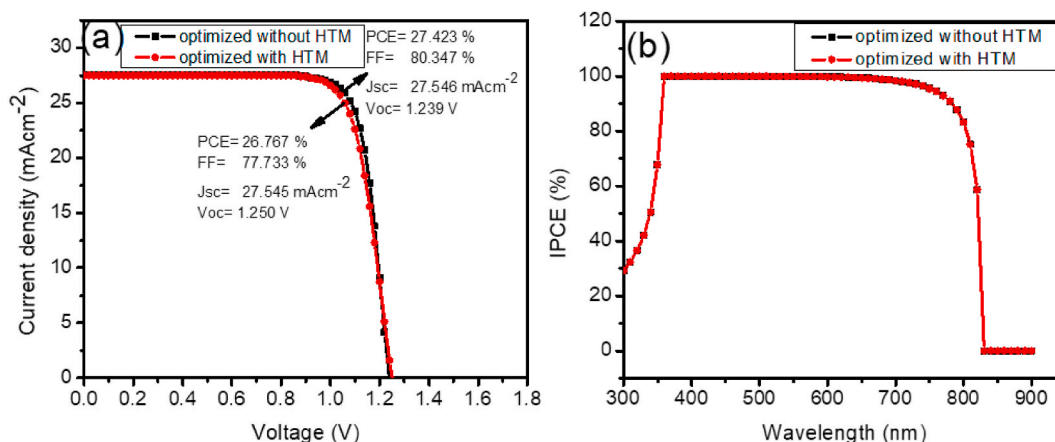


Fig. 11. (a) Optimized J - V curves for HTM and HTM-free PSC and (b) IPCE with respect to wavelength for HTM and HTM-free PSC.

Table 13

J - V characteristic data of experimental and simulated results.

Device	PCE (%)	FF (%)	J_{sc} (mA/cm ²)	V_{oc} (V)	Remark
Simulation with HTM	26.767	77.733	27.545	1.250	This work
Simulation without HTM	27.423	80.347	27.546	1.239	This work
Experimental with HTM	16.510	78.32	20.600	1.023	[7]
Simulation without HTM	25.750	89.500	23.250	1.240	[25]
Simulation with HTM	23.040	81.680	24.980	1.120	[43]
Simulation with HTM	26.667	83.005	23.232	1.383	[44]
Simulation without HTM	15.020	82.830	24.740	0.730	[45]
Experimental without HTM	15.040	61.570	23.090	1.058	[46]

Data availability statement

Data will be made available on request.

Declaration of competing interest

Authors have declared that there was no conflict of interest.

Acknowledgement

The SCAPS software package was created and made available for use by Professor Marc Burgelman and his team at the Department of Electronics and Information Systems at the University of Ghent in Belgium, for which the authors are grateful.

References

- [1] P. Moodley, Sustainable Biofuels: opportunities and challenges, *Appl. Biotechnol. Rev.* (2021) 1–20, <https://doi.org/10.1016/B978-0-12-820297-5.00003-7>.
- [2] H.K. Jun, M.A. Careem, A.K. Arof, Quantum dot-sensitized solar cells perspective and recent developments: a review of Cd chalcogenide quantum dots as sensitizers, *Renew. Sustain. Energy Rev.* 22 (2013) 148–167, <https://doi.org/10.1016/j.rser.2013.01.030>.
- [3] M. Gratzel, Photovoltaic and photoelectrochemical conversion of solar energy, *Philos. Trans. Royal Soc. A* 365 (2007) 993–1005, <https://doi.org/10.1098/rsta.2006.1963>.
- [4] I. F. Ibitoye, The millennium development goals and household energy requirements in Nigeria, *SpringerPlus* 2 (2013) 529, <https://doi.org/10.1186/2193-1801-2-529>.
- [5] E. Danladi, M. Kashif, A. Ichoja, B.B. Ayiwa, Modeling of a Sn-based HTM-free perovskite solar cell using one dimensional solar cell capacitance simulator tool, *Trans. Tianjin Univ.* 29 (2023) 62–72, <https://doi.org/10.1007/s12209-022-00343-w>.
- [6] N.J. Zadeh, M.B. Zarandi, M.R. Nateghi, Optical properties of the perovskite films deposited on meso-porous TiO₂ by one step and hot casting techniques, *Thin Solid Films* 671 (2019) 139–146, <https://doi.org/10.1016/j.tsf.2018.12.029>.
- [7] F. Behrouznejad, S. Shahbazi, N. Taghavinia, H.P. Wu, E.W.G. Diau, A study on utilizing different metals as the back contact of CH₃NH₃PbI₃ perovskite solar cells, *Journal of materials chemistry A* 4 (2016), *J. Mater. Chem.* 4 (2016) 13488–13498, <https://doi.org/10.1039/C6TA05938D>.
- [8] A. Kojima, K. Teshima, Y. Shirai, T. Miyasaka, Organometal halide perovskites as visible-light sensitizers for photovoltaic cells, *J. Am. Chem. Soc.* 131 (17) (2009) 6050–6051, <https://doi.org/10.1021/ja809598r>.
- [9] Z. Qu, F. Ma, Y. Zhao, X. Chu, S. Yu, J. You, Updated progresses in perovskite solar cells, *Chin. Phys. Lett.* 38 (2021), 107801, <https://doi.org/10.1088/0256-307X/38/10/107801>.
- [10] E. Raza, Z. Ahmad, M. Asif, F. Aziz, K. Riaz, M.Q. Mehmood, J. Bhadra, N.J. Al-Thani, Numerical modelling and performance optimization of carbon-based hole transport layer free perovskite solar cells, *Opt. Mater.* 125 (2022), 112075, <https://doi.org/10.1016/j.optmat.2022.112075>.

- [11] S. Pitchaiya, N. Eswaremoorthy, M. Natarajan, A. Santhanam, V. Asokan, V.M. Ramakrishnan, B. Rangasamy, S. Sundaram, P. Ravirajan, D. Velauthapilla, Perovskite solar cells: a porous graphitic carbon based hole transporter/counter electrode material extracted from an invasive plant species *Eichhornia crassipes*, *Sci. Rep.* 10 (2020) 6835, <https://doi.org/10.1038/s41598-020-62900-4>.
- [12] D. Bogachuk, B. Yang, J. Suo, J. D. Martineau, A. Verma, S. Narbey, M. Anaya, K. Frohna, T. Doherty, D. Müller, J.P. Herterich, S. Zouhair, A. Hagfeldt, S. D. Stranks, U. Würfel, A. Hinsch, L. Wagner, Perovskite solar cells with carbon-based electrodes—quantification of losses and strategies to overcome them, *Adv. Energy Mater.* 12 (2022), 2103128, <https://doi.org/10.1002/aenm.202103128>.
- [13] X. Rong, H. Tian, W. Bi, H. Jin, T. Zhang, D. Guo, K. Zhao, Impact of metal electrode work function of $\text{CH}_3\text{NH}_3\text{PbI}_3/\text{p-Si}$ planar heterojunction perovskite solar cells, *Sol. Energy* 158 (2017) 424–431, <https://doi.org/10.1016/j.solener.2017.08.050>.
- [14] W. Zhang, J. Xiong, S. Wang, W. Liu, J. Li, D. Wang, H. Gu, X. Wang, J. Li, Highly conductive and transparent silver grid/metal oxide hybrid electrodes for low temperature planar perovskite solar cells, *J. Power Sources* 337 (2017) 118–124, <https://doi.org/10.1016/j.jpowsour.2016.10.101>.
- [15] L. Wang, G.R. Li, Q. Zhao, X.P. Gao, Non-precious transition metals as counter electrode of perovskite solar cells, *Energy Storage Mater.* 7 (2016) 40–47, <https://doi.org/10.1016/j.ensm.2016.11.007>.
- [16] X. Xie, G. Liu, C. Xu, S. Li, Z. Liu, E.C. Lee, Tuning the work function of indiumtin-oxide electrodes for low-temperature-processed, titanium-oxide-free perovskite solar cells, *Org. Electron.* 44 (2017) 120–125, <https://doi.org/10.1016/j.orgel.2017.02.011>.
- [17] M. Chen, R.H. Zha, Z.Y. Yuan, Q.S. Jing, Z.Y. Huang, X.K. Yang, S.M. Yang, X.H. Zhao, D.L. Xu, G.D. Zou, Boron and phosphorus co-doped carbon counter electrode for efficient hole-conductor-free perovskite solar cell, *Chem. Eng. J.* 313 (2017) 791–800, <https://doi.org/10.1016/j.cej.2016.12.050>.
- [18] K. Domanski, J.P. Correa-Baena, N. Mine, M.K. Nazeeruddin, A. Abate, M. Saliba, W. Tress, A. Hagfeldt, M. Grätzel, Not all that glitters is gold: metal-migration-induced degradation in perovskite solar cells, *ACS Nano* 10 (2016) 6306–6314, <https://doi.org/10.1021/acsnano.6b02613>.
- [19] R. Rahighi, S. Gholipour, M.A. Amin, M.Z. Ansari, Hole-transport material engineering in highly durable carbon-based perovskite photovoltaic devices, *Nanomaterials* 13 (2023) 1417, <https://doi.org/10.3390/nano13081417>.
- [20] L. Feng, J. Zhu, J. Wei, Y. Li, M. Lv, S. Yang, B. Zhang, J. Yao, S. Dai, Numerical simulation: toward the design of high-efficiency planar perovskite solar cells, *Appl. Phys. Lett.* 104 (2014), 253508, <https://doi.org/10.1063/1.4885367>.
- [21] N. Fakhri, N.M. Salay, F.S. Gholami, S. SaeidNahaei, S.N. Park, S.B. Rhee, Simulation of perovskite solar cells optimized by the inverse planar method in SILVACO: 3D electrical and optical models, *Energies* 14 (2021) 5944, <https://doi.org/10.3390/en14185944>.
- [22] S. Zandi, P. Saxena, N.E. Gorji, Numerical simulation of heat distribution in RGO-contacted perovskite solar cells using COMSOL, *Sol. Energy* 197 (2020) 105–110, <https://doi.org/10.1016/j.solener.2019.12.050>.
- [23] E. Danladi, A.O. Salawu, M.O. Abdulmalik, E.D. Onoja, E.E. Onwoke, D.S. Adepehin, Optimization of absorber and ETM layer thickness for enhanced tin based perovskite solar cell performance using SCAPS-1D software, *PHYSICS Access* 2 (1) (2022) 1–11, <https://doi.org/10.47514/phyaccess.2022.2.1.001>.
- [24] T. Minemoto, M. Murata, Impact of work function of back contact of perovskite solar cells without hole transport material analyzed by device simulation, *Curr. Appl. Phys.* 14 (11) (2014) 1428–1433, <https://doi.org/10.1016/j.cap.2014.08.002>.
- [25] E. Danladi, A. Shuaibu, M.S. Ahmad, J. Tasiu, Numerical modeling and analysis of HTM-free heterojunction solar cell using SCAPS-1D, *East Eur. J. Phys.* 2 (2021) 135–145, <https://doi.org/10.26565/2312-4334-2021-2-11>.
- [26] E. Danladi, M.Y. Onimisi, S. Garba, R.U. Ugbe, J.A. Owolabi, O.O. Ige, G.J. Ibeh, A.O. Muhammed, Simulation and optimization of lead-based perovskite solar cells with cuprous oxide as a p-type inorganic layer, *Journal of the Nigerian Society of Physical Sciences* 1 (1) (2019) 72–81, <https://doi.org/10.46481/jnps.2019.13>.
- [27] P. Tiwari, M.F. Alotaibi, Y. Al-Hadeethi, V. Srivastava, B. Arkook, Sadanand, P. Lohia, D.K. Dwivedi, A. Umar, H. Algadi, S. Bascoutas, Design and simulation of efficient SnS-based solar cell using spiro-OMeTAD as hole transport layer, *Nanomaterials* 12 (2022) 2506, <https://doi.org/10.3390/nano12142506>.
- [28] M. Liu, M.B. Johnston, H.J. Snaith, Efficient planar heterojunction perovskite solar cells by vapour deposition, *Nature* 501 (2013) 395–398, <https://doi.org/10.1038/nature12509>.
- [29] D. Liu, T.L. Kelly, Perovskite solar cells with a planar heterojunction structure prepared using room-temperature solution processing techniques, *Nature Photon* 8 (2013) 133–138, <https://doi.org/10.1038/nphoton.2013.342>.
- [30] X. Liu, C. Wang, L. Lyu, C. Wang, Z. Xiao, C. Bi, J. Huang, Y. Gao, Electronic structures at the interface between Au and $\text{CH}_3\text{NH}_3\text{PbI}_3$, *Phys. Chem. Chem. Phys.* 17 (2015) 896–902, <https://doi.org/10.1039/C4CP03842H>.
- [31] F. Zhang, X. Yang, H. Wang, M. Cheng, J. Zhao, L. Sun, Structure engineering of hole-conductor free perovskite based solar cells with low-temperature-processed commercial carbon paste as cathode, *ACS Appl. Mater. Interfaces* 6 (8) (2014) 16140–16146, <https://doi.org/10.1021/am504175x>.
- [32] L. Etgar, P. Gao, Z.S. Xue, Q. Peng, A.K. Chandiran, B. Liu, M.K. Nazeeruddin, M. Grätzel, Mesoscopic $\text{CH}_3\text{NH}_3\text{PbI}_3/\text{TiO}_2$ heterojunction solar cells, *J. Am. Chem. Soc.* 134 (42) (2012) 17396–17399, <https://doi.org/10.1021/ja307789s>.
- [33] W.A. Laban, L. Etgar, Depleted hole conductor-free lead halide iodide heterojunction solar cells, *Energy Environ. Sci.* 6 (2013) 3249–3253, <https://doi.org/10.1039/C3EE42282H>.
- [34] S. Gamliel, A. Dymshits, S. Aharon, E. Terkieltaub, L. Etgar, Micrometer sized perovskite crystals in planar hole conductor free solar cells, *J. Phys. Chem. C* 119 (2015) 19722–19728, <https://doi.org/10.1021/acs.jpcc.5b07554>.
- [35] A. Dymshits, A. Rotem, L. Etgar, High voltage in hole conductor free organo metal halide perovskite solar cells, *J. Mater. Chem.* 2 (2014) 20776–20781, <https://doi.org/10.1039/C4TA05613B>.
- [36] W.J. Yin, T. Shi, Y. Yan, Unusual defect physics in $\text{CH}_3\text{NH}_3\text{PbI}_3$ perovskite solar cell absorber, *Appl. Phys. Lett.* 104 (2014), 063903, <https://doi.org/10.1063/1.4864778>.
- [37] E.M. Miller, Y. Zhao, C.C. Mercado, S.K. Saha, J.M. Luther, K. Zhu, V. Stevanovic, C.L. Perkins, J.V. de Lagemaat, Substrate-controlled band positions in $\text{CH}_3\text{NH}_3\text{PbI}_3$ perovskite films, *Phys. Chem. Chem. Phys.* 16 (2014) 22122–22130, <https://doi.org/10.1039/C4CP03533J>.
- [38] I. Jeong, H.J. Kim, B.S. Lee, H.J. Son, J.Y. Kim, D.K. Lee, D.E. Kim, J. Lee, M.J. Ko, Highly efficient perovskite solar cells on mechanically durable molybdenum cathode, *Nano Energy* 17 (2015) 131–139, <https://doi.org/10.1016/j.nanoen.2015.07.025>.
- [39] S. Ryu, J.H. Noh, N.J. Jeon, Y.C. Kim, W.S. Yang, J. Seo, S.I. Seok, Voltage output of efficient perovskite solar cells with high open-circuit voltage and fill factor, *Energy Environ. Sci.* 7 (2014) 2614–2618, <https://doi.org/10.1039/C4EE00762J>.
- [40] Y. Xu, Z. Lin, W. Wei, Y. Hao, S. Liu, J. Ouyang, J. Chang, Recent progress of electrode materials for flexible perovskite solar cells, *Nano-Micro Lett.* 14 (2022) 117, <https://doi.org/10.1007/s40820-022-00859-9>.
- [41] G. Pindolia, S.M. Shinde, P.K. Jha, Optimization of an inorganic lead free RbGeI_3 based perovskite solar cell by SCAPS-1D simulation, *Sol. Energy* 236 (2022) 802–821, <https://doi.org/10.1016/j.solener.2022.03.053>.
- [42] J. Barbé, M.L. Tietze, M. Neophytou, B. Murali, E. Alarousu, A.E. Labban, F. Abulikemu, W. Yue, O.F. Mohammed, I. McCulluch, A. Amassian, S.D. Gobbo, Amorphous tin oxide as a low-temperature-processed electrontransport layer for organic and hybrid perovskite solar cells, *ACS Appl. Mater. Interfaces* 9 (2017) 11828–11836, <https://doi.org/10.1021/acsami.6b13675>.
- [43] Y. Raoui, H. Ez-Zahraouy, N. Tahiri, O. El Bounagui, O. Ahmad, S. Kazim, Performance analysis of MAPbI_3 based perovskite solar cells employing diverse charge selective contacts: simulation study, *Sol. Energy* 193 (2019) 948–955, <https://doi.org/10.1016/j.solener.2019.10.009>.
- [44] E. Danladi, A.C. Egbugha, R.C. Obasi, N.N. Tasie, C.U. Achem, I.S. Haruna, L.O. Ezech, Defect and doping concentration study with series and shunt resistance influence on graphene modified perovskite solar cell: a numerical investigation in SCAPS-1D framework, *J. Indian Chem. Soc.* 100 (2023), 101001, <https://doi.org/10.1016/j.jics.2023.101001>.
- [45] L. Lin, L. Jiang, Y. Qiu, Y. Yu, Modeling and analysis of HTM-free perovskite solar cells based on ZnO electron transport layer, Superlattices and Microstruct 104 (2017) 167–177, <https://doi.org/10.1016/j.spmi.2017.02.028>.
- [46] J. Zhou, Z. Ye, J. Hou, J. Wu, Y.Z. Zheng, X. Tao, (2018). Efficient ambient-air-stable HTM-free carbon-based perovskite solar cells with hybrid 2D-3D lead halide photoabsorber, *J. Mater. Chem.* 6 (2018) 22626–22635, <https://doi.org/10.1039/C8TA07836J>.